

Structure of ultrathin amorphous carbon films deposited by filtered cathodic vacuum arc for magnetic recording

N. Wang and K. Komvopoulos

Department of Mechanical Engineering, University of California, Berkeley, California, 94720

Abstract

Amorphous carbon (*a*-C) films deposited by filtered cathodic vacuum arc (FCVA) exhibit superior mechanical properties and wear resistance than *a*-C films deposited by other methods, such as sputtering, electron-beam evaporation, and chemical vapor deposition. Because of continuously increasing demands for protective ultrathin *a*-C films in various leading technologies, such as information storage and optoelectronics, knowledge of the structure of such films is of high technological and scientific importance. In this study, ~20-nm-thick *a*-C films deposited on Si(100) by the FCVA method were examined by high-resolution transmission electron microscopy, electron energy loss spectroscopy, and X-ray photoelectron spectroscopy. Results of the plasmon excitation energy shift and the through-thickness elemental concentration show the formation of a multilayered *a*-C film structure consisting of an interface layer consisting of C, Si, and, possibly, SiC, a buffer layer with continuously increasing sp^3 fraction, a relatively thicker layer of the bulk film of constant sp^3 content, and an ultrathin surface layer rich in sp^2 hybridization. A detailed study of the C K-edge spectrum suggests that the buffer layer between the interface layer and the bulk film is due to partial backscattering of the C^+ ions interacting with the heavy atoms of the silicon substrate. The results of this study provide insight into the minimum thickness of *a*-C films synthesized under optimum substrate bias FCVA conditions.

I. INTRODUCTION

Filtered cathodic vacuum arc (FCVA) is one of the most effective ultrathin-film deposition methods. Amorphous carbon (*a*-C) films synthesized by the FCVA method exhibit high purity, excellent uniformity, very small roughness, high hardness, low friction, and good wear and corrosion resistance.¹⁻⁴ The superior nanomechanical/tribological properties of these *a*-C films, demonstrated by nanoindentation and nanoscratching experiments,⁵⁻⁸ are mainly attributed to the high fraction of tetrahedral (*sp*³) carbon atom hybridization. The structures of various types of carbon films have been extensively studied by X-ray photoelectron spectroscopy (XPS) and Raman spectroscopy.⁸⁻¹⁴ However, because the information obtained by these methods is averaged over a depth of a few nanometers, XPS and Raman spectroscopy cannot provide information about the through-thickness structure of nanometer-thick *a*-C films. Although elemental depth profiles may be obtained with *in situ* high-energy Ar⁺ plasma sputtering during XPS, it is difficult to accurately calibrate and control the sputtering rate of ultrathin films. In addition, the intense energetic Ar⁺ ion bombardment during sputter etching may alter the film structure.^{15,16} Detailed structural analysis of ultrathin films requires cross-section transmission electron microscopy (TEM) samples and microanalysis techniques with a very high spatial resolution, such as electron energy loss spectroscopy (EELS).

Previous EELS studies of *a*-C films deposited on silicon by the FCVA method under different substrate bias conditions have revealed a layered film structure consisting of an interface layer, the bulk film, and a surface layer.^{11,17-20} According to the subplantation model,²¹ the interface layer is less dense than the bulk film and its formation is a result of partial backscattering of the C⁺ ions impinging onto the heavy Si atoms, the bulk film is due to C⁺ ion subplantation and is characterized by a high compressive stress, and the surface layer is dominated by trigonal (*sp*²) carbon atom hybridization and is also less dense than the bulk film. The thickness of the interface and surface layers depends on the penetration depth of the C⁺ ions, which is a function of the C⁺ ion energy.¹⁷⁻¹⁹ Surface and interface layers of thickness equal to ~12 and ~3 nm have been reported for 55-nm-thick *a*-C films deposited on Si(100) by FCVA under plasma conditions of 90 eV C⁺ ion energy.¹⁷ However, significantly thinner surface layers of

thickness between 0.4 ± 0.2 and 1.3 ± 0.3 nm have been observed in other studies for C^+ ion energy of 35 and 320 eV, respectively.^{18,19}

The quality of FCVA-deposited *a*-C films strongly depends on the C^+ ion energy. Intensification of collision cascades between C^+ ions and substrate atoms with the increase of the C^+ ion energy yields localized high pressures that are conducive to sp^3 hybridization. However, high C^+ ion energy may also promote thermal relaxation, resulting in sp^3 -to- sp^2 rehybridization. Because of these competing processes, there is an optimum C^+ ion energy (typically, ~ 120 eV)^{1,22} for depositing *a*-C films with maximum sp^3 content. The majority of previous studies dealing with the structure of FCVA-deposited *a*-C films were focused on the effect of substrate bias but not the optimum C^+ ion energy. Therefore, a principal objective of this study was to perform a detailed analysis of the through-thickness structure of ultrathin *a*-C films synthesized by the FCVA technique under optimum C^+ ion energy conditions. Because the energy of C^+ ions generated by arcing is ~ 20 eV,²³⁻²⁵ a substrate bias voltage of -100 V was used to obtain C^+ ion energy of ~ 120 eV during film deposition. High-resolution transmission electron microscopy (HRTEM) and analytical EELS were used to study the *a*-C film structure. Low- and high (core)-loss EELS spectra of Si and C were analyzed to determine the elemental content and through-thickness structure of ~ 20 -nm-thick *a*-C films. Calculations of atomic carbon hybridization based on EELS spectra were used to track the film structure evolution. The average content of carbon hybridization in the top few nanometers of the *a*-C film determined from EELS analysis was validated by XPS results.

II. EXPERIMENTAL METHODS

A. Film deposition by filtered cathodic vacuum arc

Commercially available p-type Si(100) wafers were sectioned into 10×10 mm² substrates, which were cleaned by rinsing in isopropanol and acetone for 10 min, respectively, and dried by blowing nitrogen gas. After pumping down the FCVA chamber to $< 5 \times 10^{-7}$ Torr and, subsequently, introducing Ar gas that increased the chamber pressure to 2×10^{-4} Torr, the substrate was sputtered for 2 min with 500-eV Ar^+ ions generated by a 64-mm Kaufman ion source to remove the native SiO_2 layer. The

incidence angle of the bombarding Ar^+ ions was fixed at 60° , as measured from the normal to the substrate surface. After reaching a base pressure of $<5 \times 10^{-7}$ Torr, carbon plasma was generated by arcing on the cathode (99.99% pure graphite) surface and stabilized by a cusp-configuration magnetic field applied to the cathode.²⁶ Any macroparticles and/or droplets were filtered out by the magnetic field of electromagnetic coils having an S-shape duct configuration. At the exit of the filter structure, the carbon plasma comprised only high-purity ($\sim 99.99\%$) C^+ ions. To control the C^+ ion energy during film deposition, a pulsed bias voltage of -100 V (time-average magnitude) and a 25 kHz frequency was applied to the substrate holder. To obtain ultrathin *a*-C films, the deposition time was set at 30 s. FCVA deposition under plasma conditions of -100 V substrate bias produces ultrathin *a*-C films with the highest sp^3 fraction and nanohardness.⁸ To enhance the film uniformity in the radial direction, the substrate was rotated at 60 rpm during film deposition. More details about the FCVA system used in this study can be found elsewhere.²⁶

B. Transmission electron microscopy and electron energy-loss spectroscopy

Cross-sectional TEM samples were prepared by mechanical grinding and dimpling and surface finished by ion milling. The film samples were cleaved into two halves and glued face-to-face using M-bond 610 epoxy. To ensure that the EELS carbon signal was only due to the *a*-C film, a thin Au layer was evaporated onto the sample surface before sample bonding. More details about the preparation of the TEM samples can be found elsewhere.^{27,28} To minimize surface adsorption of hydrocarbon from the ambient, the TEM samples were kept in a vacuum of $<10^{-5}$ Torr and observed with the TEM within two days from fabrication.

HRTEM images and EELS spectra were obtained with a FEI Tecnai (F20 UT) spectrometer operated at 200 kV, using a CCD camera (2048×2048 pixels) positioned 42 mm behind the Gatan imaging filter. The spatial resolution of the scanning TEM (STEM), without a monochromator, is ~ 0.14 nm. A 13.5-mrad C2 semi-angle and a 100- μm C2 aperture were used in this study. The EELS collection semi-angle was set at 47 mrad. Using the full width at half maximum (FWHM) of the zero-loss peak

(ZLP), the energy resolution was found equal to 0.58 eV, which is sufficiently small for distinguishing sp^2 from sp^3 hybridizations since their band gap difference is about 0.8–0.9 eV. ZLP and low-loss spectra were collected in 0.02 s. Because the core-edge signal is significantly weaker than elastic scattering, the Si $L_{2,3}$ -edge and the C K-edge were collected for 4 s in order to enhance the observation of fine structure details.

C. X-ray photoelectron spectroscopy

A PHI 5400 XPS system (Physical Electronics, Chanhassen, MN) with conventional (non-monochromatic) Al-K α radiation of 1486.6 eV energy and 4.8 eV work function operated under a vacuum pressure of $<2 \times 10^{-8}$ Torr was used to study carbon atom hybridization in the *a*-C films. The system has a spatial resolution of 0.5 mm and energy resolution of 0.7 eV. The samples were not cleaned before the XPS analysis to preserve their surface elemental and chemical state. Multiplex narrow-scan spectra of the C1s core-level peak were acquired with pass energy of 37.75 eV, using a channel width of 0.1 eV/step and acquisition time fixed at 50 ms/step. Spectra were collected after 60 sweeps in the binding energy range of 280–292 eV. Three spectra were obtained from difference locations on the same sample to ensure consistency. Charging effects on the samples were not observed during the XPS measurements.

III. RESULTS AND DISCUSSION

The removal of the native SiO₂ layer by the highly energetic Ar⁺ ions may cause amorphization of the Si(100) substrate. The structure of the silicon substrate is important because it controls the initial growth of the carbon film. The bright-field, phase-contrast HRTEM image of the Si(100) substrate obtained after sputter cleaning with 500-eV Ar⁺ ions (Fig. 1A) shows the formation of a 2.5 ± 0.5 -nm-thick surface layer of amorphous silicon (*a*-Si). The difference in brightness is mainly due to density differences between Si(100) and *a*-Si. The HRTEM image of the *a*-C film deposited on the cleaned Si(100) substrate in 30 s under a substrate bias voltage of –100 V (Fig. 1B) shows the formation of a $\sim 20.9 \pm 0.3$ -nm-thick *a*-C film, including an approximately 3-nm-thick interface layer of intermixed C, Si, and, possibly, SiC.

The elemental composition of the *a*-C film shown in Fig. 1B was studied by analytical EELS. This technique uses the energy loss of electrons passing through the specimen to determine the chemical composition and electronic structure of the specimen. Electron energy loss is mainly due to inelastic electron-electron collisions.^{29,30} Beam electrons interacting with electrons of the conduction and/or valence bands of the specimen material are detected in the low-energy loss range (typically, <50 eV) of the EELS spectrum. Because the electronic properties of a material are controlled by the weakly bound electrons in the conduction and valence bands, the distribution of the EELS spectrum below 50 eV provides information about specific phases or features in the TEM image.

Assuming free electrons, i.e., not bound to any specific atom or ion, the energy loss E_p of the beam electrons generating a plasmon frequency ω_p is given by²⁹

$$E_p = \frac{h}{2\pi} \omega_p = \frac{h}{2\pi} \left(\frac{ne^2}{\epsilon_0 m} \right)^{1/2} \quad (1)$$

where h is the Planck's constant, e and m are the electron charge and mass, respectively, ϵ_0 is the permittivity of free space, and n is the electron density. For single-crystal Si and *a*-C with a low sp^3 fraction, the plasmon peak position is typically at ~16–17 eV^{31,32} and 24–25 eV,^{33,34} respectively, while for graphitic carbon and amorphous diamond the plasmon peak position is at 26–27 and 30–33 eV, respectively.^{34,35} The film structure can be examined by studying the through-thickness variation of the plasmon peak position.

Since the energy-loss spectrometer is susceptible to external fields and the ZLP shifts over time, each EELS spectrum was calibrated by shifting the ZLP to the zero position. Figure 2A shows a cross-sectional STEM image and EELS spectra obtained from different locations in the depth direction of the TEM sample. Spectrum (a) with a plasmon peak at ~16 eV corresponds to the Si(100) substrate. Location (b) is on the line of maximum contrast between Si(100) and amorphous structures. The plasmon peak position in spectrum (b) is slightly above 16 eV and its reduced intensity indicates a weakening of the Si signal. The large shift of the plasmon peak of spectrum (c) to ~21.7 eV is attributed to the contribution of plasmon signals from both Si and C. The contribution of Si features to the electron energy loss decays,

while that of C features intensifies with increasing depth distance. The change from spectrum (b) to spectrum (c) reveals the existence of a thin interfacial region with gradually changing C and Si contents. The spectra obtained away from this interfacial region, i.e., spectra (d) and (e), have very similar distributions and a plasmon peak centered at ~ 29 eV. These spectra correspond to the bulk of the carbon film and are representative of steady-state film growth. A plasmon peak position close to that of diamond indicates a high fraction of sp^3 hybridization. The plasmon peak position in spectrum (f) corresponding to the film surface is at ~ 24 eV, which is close to that of graphitized carbon. This implies that the surface structure of the carbon film is dominated by sp^2 hybridization. The gold layer shows a very weak plasmon signal (spectrum (g)), indicating insignificant hydrocarbon contamination of the TEM specimen. The plasmon peak in the epoxy spectrum (h) is centered at ~ 22 eV.

To quantify the change in the plasmon peak position in the depth direction of the cross-sectional TEM sample, EELS spectra were obtained at depth increments of 2 nm. Figure 2B shows the variation of the plasmon peak position in the depth sample direction after ZLP calibration. The zero-depth position corresponds to the location exhibiting the highest contrast between carbon film and the gold layer (i.e., film surface). The low-energy-loss range (< 50 eV) reveals a multilayered structure consisting of single-crystal Si, amorphous C, Si, and, possibly SiC (interface layer), graphite-like carbon (buffer layer), diamond-like carbon (bulk film), and graphite-like carbon (surface layer).

The high-energy-loss range (> 50 eV) contains information about inelastic interactions between beam electrons and inner or core-shell electrons. Thus, information about the elemental composition can be extracted from the ionization edges. Since the interface layer was found to consist of C and Si, its elemental concentration was determined from the core-loss energy of the Si $L_{2,3}$ peak centered at 99 eV along a 20-nm-long scan line using a step increment of 1 nm. The silicon concentration was calculated as the ratio of the Si $L_{2,3}$ peak intensity in the spectrum of the interface layer to that in the spectrum of the single-crystal Si(100) region. Figure 3A shows high-energy-loss spectra obtained from different locations after background subtraction. Spectra (a) and (b) correspond to the Si(100) substrate, and their similar distributions and strength intensities indicate similar structures and compositions. A comparison of

spectra (c)–(e) shows a profound decrease in the intensity of the Si $L_{2,3}$ peak. This trend is attributed to the continuously decreasing Si concentration through the interface layer and toward the interface with the bulk film. The normalized intensity of the Si $L_{2,3}$ peak, defined as the ratio of the area under the EELS spectra from 94 to 104 eV to the corresponding area of the Si(100) spectrum, is shown as a function of depth in Fig. 3B. Because all of the measurements were obtained along a very short distance (20 nm), variations in the specimen thickness were negligible and the variation of the signal intensity is only due to the relative concentration of Si. The transition band has a thickness of ~ 4.5 nm, which is slightly larger than that of the *a*-Si layer on the Si(100) substrate (Fig. 1A). This difference may be attributed to the bombardment effect of energetic C^+ ions in the initial stage of film deposition, resulting in the implantation of C into the Si substrate and, in turn, thickening of the *a*-Si layer at the interface of the Si(100) substrate and the *a*-C film.

Figure 4 shows high-energy-loss spectra of the C K-edge obtained in the depth direction of the cross-sectional TEM sample using a step size of 0.5 nm. The locations from where spectra were obtained are very close to those shown in Fig. 2A. Spectra locations were slightly offset during the acquisition of the low- and high-energy-loss spectra to avoid sample damage and/or carbon re-deposition from previous spectra acquisitions. All C K-edge spectra were calibrated by centering the π^* peak at 285 eV. As expected, spectra (a) and (b) of the Si(100) substrate are featureless. However, spectrum (c) of the interface layer contains a small π^* peak and a well-defined σ^* peak, with both peaks attributed to electron beam interactions with C atoms. The similar distributions and significantly intensified signal in spectra (d) and (e) indicate a high carbon concentration in the bulk film. The decrease of the signal intensity at the film surface and the dominance of the π^* peak in the corresponding spectrum (f) suggest that carbon atom hybridization at the film surface is predominantly sp^2 . The gold layer does not produce C K-edge signal (spectrum (g)), while the epoxy shows a strong π^* peak and a weak σ^* peak (spectrum (h)). Information about the chemical composition and carbon hybridization of the *a*-C film derived from Fig. 4 is in good agreement with that obtained from Fig. 2A.

EELS spectra in the range of 280–305 eV were analyzed to determine the sp^2 and sp^3 fractions in the a -C film. Figure 5 shows a representative high-energy-loss spectrum of the a -C bulk film. The location in the bulk film from where the spectrum was obtained is marked by a circle in the STEM image shown on the right. The peak at 285 eV is due to the excitation of electrons from the ground-state 1s core levels to the vacant π^* states. The π^* peak is fitted with a Gaussian distribution, whereas the σ^* peak is integrated within a small energy window from 290 to 305 eV in order to minimize effects of plural scattering. The area ratio of these two peaks is proportional to the relative number of the π^* and σ^* orbitals.³⁶ The fraction of sp^2 bonded carbon atoms x is given by³⁶

$$\frac{(\pi^*/\sigma^*)_{\text{film}}}{(\pi^*/\sigma^*)_{\text{std}}} = \frac{3x}{4-x} \quad (2)$$

where the standard sample is assumed to be pure graphite with 100% sp^2 atomic carbon hybridization.

Figure 6A shows a depth profile of the sp^3 fraction calculated from the C K-edge spectra using Eq. (2). Similar to the Si $L_{2,3}$ -edge, the intensity of the C K-edge was calculated from an integration performed from 280 to 305 eV. The depth profile of the normalized C K-edge intensity is shown in Fig. 6B. The sp^3 atomic fraction (Fig. 6A) and the carbon concentration (Fig. 6B) reveal the existence of six distinctly different regions through the cross-sectional sample. Data points of the sp^3 fraction are not shown in range I because the C signal intensity is almost zero in the Si(100) substrate. Region II represents the ~4.5-nm-thick interface layer and is characterized by an increasing C concentration and a merely constant sp^3 fraction of $\sim 45.0 \pm 5.8\%$. In the ~2-nm-thick carbon layer above the interface layer (regime III), the carbon intensity reaches a maximum, while the sp^3 fraction increases from ~45% to ~70%. The next region IV corresponds to a ~12.5-nm-thick bulk a -C film with a constant sp^3 fraction equal to $73.2 \pm 1.9\%$. The sp^3 fraction in the ~1.5-nm-thick surface layer of the a -C film (region V) rapidly decreases to $50.6 \pm 3.3\%$ toward the surface. Region VI represents a gold particle separating the a -C film from the epoxy glue. Because of the low carbon signal produced by the gold particle, data of the sp^3 fraction were also omitted from region VI.

Different from the traditional three-layer model of carbon films deposited by energetic carbon ions,^{17-19,21} a fourth (buffer) layer of thickness ~ 2 nm was discovered between the interface layer consisting of intermixed C and Si and the bulk of the *a*-C film. The buffer layer exhibits a very high carbon concentration ($>95\%$) and its sp^3 fraction increases from the interface with the interface layer toward the interface with the bulk film. The observed four-layer structure of the ultrathin *a*-C film can be explained by the following film-growth model. The initial stage of film deposition is dominated by backscattering and penetration of energetic C^+ ions into the *a*-Si surface layer of the substrate, resulting in the growth of an interface (intermixing) amorphous layer consisting of C, Si, and, possibly, SiC. This interface layer exhibits a relatively low sp^3 fraction because of the low carbon concentration. Although the structure of SiC is similar to that of an sp^3 hybridized carbon structure, the ionization energy of C1s core-level electrons of carbidic components is usually in the range of 282.3–283.4 eV with a broad FWHM of ~ 2 eV,³⁷ which is very close and, therefore, hardly distinguishable from the ionization energy of sp^2 carbon atom hybridization. This explains the low sp^3 concentration in the interface layer (region II), despite of the possible existence of SiC. The arrival of more C^+ ions leads to the formation of a thin buffer layer of pure carbon (regime III) on top of the interface layer. However, because the C^+ ion penetration depth exceeds the initial thickness of the buffer layer, some of the impinging C^+ ions are backscattered by the Si atoms in the interface layer. Since the probability of C^+ ion-Si atom interaction decreases with the thickness of the buffer layer, the sp^3 fraction exhibits a positive gradient toward the interface of the buffer layer with the bulk film. When the thickness of the buffer layer exceeds the penetration depth range of the C^+ ions, only carbon-carbon interactions occur and the localized compressive stresses induced by the subplantation process promote the occurrence of sp^3 hybridization. The resulting steady-state film growth conditions lead to the formation of the bulk film with constant and high sp^3 content (regime IV). However, because the bulk film surface experiences relatively less C^+ ion bombardment, a surface layer with increased sp^2 content and thickness about equal to the C^+ ion penetration (regime V) is produced during the final stage of film deposition.

The sp^3 fraction was also calculated from the C1s core-level XPS spectrum shown in Fig. 7. The C1s peak was deconvoluted by five Gaussian distributions corresponding to sp^1 , sp^2 , sp^3 , C–O, and C=O carbon bonding. Details about the deconvolution method can be found elsewhere.^{27,38} The sp^3 fraction was found to be $73.9 \pm 1.5\%$, which is close to that ($73.2 \pm 1.9\%$) calculated from the EELS C K-edge spectrum. Because the sampling depth in the XPS is ~ 10 nm, the XPS signal was predominantly from the bulk film and the existence of the much thinner interface, buffer, and surface layers possessing significantly lower sp^3 fractions cannot be captured by the XPS.

IV. CONCLUSIONS

The structure of ultrathin *a*-C films deposited by the FCVA method under plasma conditions of optimum substrate bias voltage was studied in the light of TEM, EELS, and XPS results. The plasmon excitation energy position in low-energy-loss spectra revealed a multilayered film structure. Depth profiles of carbon atom concentration and sp^3 carbon hybridization obtained from the analysis of high-energy-loss spectra showed that the film structure consists of a ~ 4.5 -nm-thick interface layer (a mixture of C, Si, and, possibly, SiC), a ~ 2 -nm-thick buffer layer of pure carbon with outward increasing sp^3 fraction, a ~ 12.5 -nm-thick bulk film of constant and high sp^3 fraction ($\sim 74\%$), and a ~ 1.5 -nm-thick surface layer of high sp^2 content. XPS results confirmed the sp^3 fraction calculated from the C K-edge EELS spectrum. The buffer and surface layers possess similar thickness, which depends on the C^+ ion penetration depth that is controlled by the kinetic energy of the bombarding C^+ ions. The results of this study show that the minimum thickness of *a*-C films synthesized by the FCVA method under optimum substrate bias (-100 V) plasma conditions is equal to $3\text{--}3.5$ nm, which is the total thickness of the buffer and surface layers.

ACKNOWLEDGMENTS

This research was funded in part by the Computer Mechanics Laboratory (CML). TEM and XPS studies were performed at the National Center for Electron Microscopy and the Molecular Foundry, respectively, of the Lawrence Berkeley National Laboratory.

REFERENCES

1. J. Robertson: Diamond-like amorphous carbon. *Mater. Sci. Eng. R* **37**, 129 (2002).
2. O.R. Monteiro: Thin film synthesis by energetic condensation. *Annu. Rev. Mater. Res.* **31**, 111 (2001).
3. I.G. Brown: Cathodic arc deposition of films. *Annu. Rev. Mater. Sci.* **28**, 243 (1998).
4. A.A. Voevodin and M.S. Donley: Preparation of amorphous diamond-like carbon by pulsed laser deposition: a critical review. *Surf. Coat. Technol.* **82**, 199 (1996).
5. M.K. Fung, K.H. Lai, C.Y. Chan, I. Bello, C.S. Lee, S.T. Lee, D.S. Mao, and X. Wang: Mechanical properties and corrosion studies of amorphous carbon on magnetic disks prepared by ECR plasma technique. *Thin Solid Films* **368**, 198 (2000).
6. R. Hauert: An overview on the tribological behavior of diamond-like carbon in technical and medical applications. *Tribol. Int.* **37**, 991 (2004).
7. A. Erdemir and C. Donnet: Tribology of diamond-like carbon films: recent progress and future prospects. *J. Phys. D: Appl. Phys.* **39**, R311 (2006).
8. H.-S. Zhang and K. Komvopoulos: Synthesis of ultrathin carbon films by direct current filtered cathodic vacuum arc. *J. Appl. Phys.* **105**, 083305 (2009).
9. J. Díaz, G. Paolicelli, S. Ferrer, and F. Comin. Separation of the sp^3 and sp^2 components in the C1s photoemission spectra of amorphous carbon films. *Phys. Rev. B* **54**, 8064 (1996).
10. N. Yasui, H. Inaba, K. Furusawa, M. Saito, and N. Ohtake: Characterization of head overcoat for 1 Tb/in² magnetic recording. *IEEE Trans. Magn.* **45**, 805 (2009).

11. J. Zhu, J. Han, X. Han, H.I. Schlaberg, and J. Wang: sp^3 -rich deposition conditions and growth mechanism of tetrahedral amorphous carbon films deposited using filtered arc. *J. Appl. Phys.* **104**, 013512 (2008).
12. A.C. Ferrari and J. Robertson: Raman spectroscopy of amorphous, nanostructured, diamond-like carbon, and nanodiamond. *Phil. Trans. R. Soc. London A* **362**, 2477 (2004).
13. A.C. Ferrari and J. Robertson: Interpretation of Raman spectra of disordered and amorphous carbon. *Phys. Rev. B* **61**, 14095 (2000).
14. D.S. Knight and W.B. White: Characterization of diamond films by Raman spectroscopy. *J. Mater. Res.* **4**, 385 (1989).
15. S. Oswald and R. Reiche: Binding state information from XPS depth profiling: capabilities and limits. *Appl. Surf. Sci.* **179**, 307 (2001).
16. P.R. Poudel, P.P. Poudel, B. Rout, M. El Bouanani, and F.D. McDaniel: An XPS study to investigate the dependence of carbon ion fluences in the formation of buried SiC. *Nucl. Instrum. Methods Phys. Res. B* **283**, 93 (2012).
17. M.P. Siegal, P.N. Provencio, D.R. Tallant, R.L. Simpson, B. Kleinsorge, and W.I. Milne: Bonding topologies in diamondlike amorphous-carbon films. *Appl. Phys. Lett.* **76**, 2047 (2000).
18. C.A. Davis, G.A.J. Amaratunga, and K.M. Knowles: Growth mechanism and cross-sectional structure of tetrahedral amorphous carbon thin films. *Phys. Rev. Lett.* **80**, 3280 (1998).
19. C.A. Davis, K.M. Knowles, and G.A.J. Amaratunga: Cross-sectional structure of tetrahedral amorphous carbon thin films. *Surf. Coat. Technol.* **76-77**, 316 (1995).

20. E. Riedo, F. Comin, J. Chevrier, F. Schmithusen, S. Decossas, and M. Sancrotti: Structural properties and surface morphology of laser-deposited amorphous carbon and carbon nitride films. *Surf. Coat. Technol.* **125**, 124 (2000).
21. Y. Lifshitz, S.R. Kasi, J.W. Rabalais, and W. Eckstein: Subplantation model for film growth from hyperthermal species. *Phys. Rev. B* **41**, 10468 (1990).
22. G.M. Pharr, D.L. Callahan, S.D. McAdams, T.Y. Tsui, S. Anders, A. Anders, J.W. Ager III, I.G. Brown, C.S. Bhatia, S.R.P. Silva, and J. Robertson: Hardness, elastic modulus, and structure of very hard carbon films produced by cathodic-arc deposition with substrate pulse biasing. *Appl. Phys. Lett.* **68**, 779 (1996).
23. J. Robertson: Requirements of ultrathin carbon coatings for magnetic storage technology. *Tribol. Int.* **36**, 405 (2003).
24. J. Robertson: Ultrathin carbon coatings for magnetic storage technology. *Thin Solid Films* **383**, 81 (2001).
25. E. Byon and A. Anders: Ion energy distribution functions of vacuum arc plasmas. *J. Appl. Phys.* **93**, 1899 (2003).
26. H.-S. Zhang and K. Komvopoulos: Direct-current cathodic vacuum arc system with magnetic-field mechanism for plasma stabilization. *Rev. Sci. Instrum.* **79**, 073905 (2008).
27. N. Wang and K. Komvopoulos: Incidence angle effect of energetic carbon ions on deposition rate, topography, and structure of ultrathin amorphous carbon films deposited by filtered cathodic vacuum arc. *IEEE Trans. Magn.* **48**, 2220 (2012).
28. D. Wan and K. Komvopoulos: Transmission electron microscopy and electron energy loss spectroscopy analysis of ultrathin amorphous carbon films. *J. Mater. Res.* **19**, 2131 (2004).

29. D.B. Williams and C.B. Carter, *Transmission Electron Microscopy: A Textbook for Materials Science* (Springer, New York, Chapter 37, pp. 679-681, 2009).
30. R.F. Egerton, *Electron Energy-Loss Spectroscopy in the Electron Microscope* (3rd edition, Springer, New York, Chapter 3, pp. 111-229, 2011).
31. R.F. Egerton: Electron energy-loss spectroscopy in the TEM. *Rep. Prog. Phys.* **72**, 016502 (2009).
32. V. Olevano and L. Reining: Excitonic effects on the silicon plasmon resonance. *Phys. Rev. Lett.* **86**, 5962 (2001).
33. D.R. McKenzie, D. Muller, and B.A. Pailthorpe: Compressive-stress-induced formation of thin-film tetrahedral amorphous carbon. *Phys. Rev. Lett.* **67**, 773 (1991).
34. A. Duarte-Moller, F. Espinosa-Magana, R. Martinez-Sanchez, M. Avalos-Borja, G.A. Hirata, and L. Cota-Araiza: Study of different forms of carbon by analytical electron microscopy. *J. Electron Spectr. Relat. Phenom.* **104**, 61 (1999).
35. S.D. Berger, D.R. McKenzie, and P.J. Martin: EELS analysis of vacuum arc-deposited diamond-like films. *Philos. Mag. Lett.* **57**, 285 (1988).
36. J.J. Cuomo, J.P. Doyle, J. Bruley, and J.C. Liu: Sputter deposition of dense diamond-like carbon films at low temperature. *Appl. Phys. Lett.* **58**, 466 (1991).
37. R.J. Iwanowski, K. Fronc, W. Paszkowicz, and M. Heinonen: XPS and XRD study of crystalline 3C-SiC grown by sublimation method. *J. Alloys and Compounds* **286**, 143 (1999).
38. D. Wan and K. Komvopoulos: Tetrahedral and trigonal carbon atom hybridization in thin amorphous carbon films synthesized by radio-frequency sputtering. *J. Phys. Chem. C* **111**, 9891 (2007).

List of Figures

- Fig. 1 Bright-field HRTEM images of (A) the Si(100) substrate after a 2-min sputter-etching by 500-eV Ar^+ ions to remove the native SiO_2 layer and (B) the *a*-C film deposited in 30 s on the sputter-etched Si(100) substrate by the FCVA method under plasma conditions of optimum substrate bias voltage (−100 V). Interfaces are distinguished by dashed lines.
- Fig. 2 (A) EELS spectra obtained from different locations across the interface of the Si(100) substrate and the *a*-C film, shown in the *z*-contrast STEM image shown on the right. The brightest region corresponds to evaporated Au used to distinguish the surface of the *a*-C film from the epoxy surface. The spectra were calibrated by shifting the ZLP to 0 eV. Local electronic change at the atomic level is discerned. (B) Depth profile of the plasmon peak position.
- Fig. 3 (A) Variation of the Si $L_{2,3}$ -edge across the interface of the Si(100) substrate and the *a*-C film, shown in the STEM image shown on the right. The spectra were calibrated by shifting the Si $L_{2,3}$ -edge to 99 eV after background subtraction. (B) Depth profile of the normalized intensity of the Si $L_{2,3}$ -edge.
- Fig. 4 C K-edge spectra obtained from different locations across the interface of the Si(100) substrate and the *a*-C film, shown in the STEM image shown on the right. The spectra were calibrated by shifting the π^* peak of all C K-edge spectra to 285 eV after background subtraction.
- Fig. 5 Decomposition of the C K-edge spectrum of the *a*-C bulk film into π^* and σ^* peaks. The location in the bulk film from where the spectrum was obtained is marked by a circle in the STEM image shown on the right. The π^* peak is represented by a Gaussian distribution from 282 to 287.5 eV, whereas the σ^* peak is defined as the spectrum in the energy window from 290 to 305 eV.
- Fig. 6 Depth profiles of (A) the sp^3 fraction calculated from C K-edge spectra and (B) normalized intensity of the C K-edge. Boundaries of neighboring regimes are distinguished by dashed lines.
- Fig. 7 C1s core-level XPS spectrum of *a*-C film after Shirley inelastic background subtraction with five fitted Gaussian distributions corresponding to sp^1 , sp^2 , sp^3 , C–O, and C=O carbon bonding.

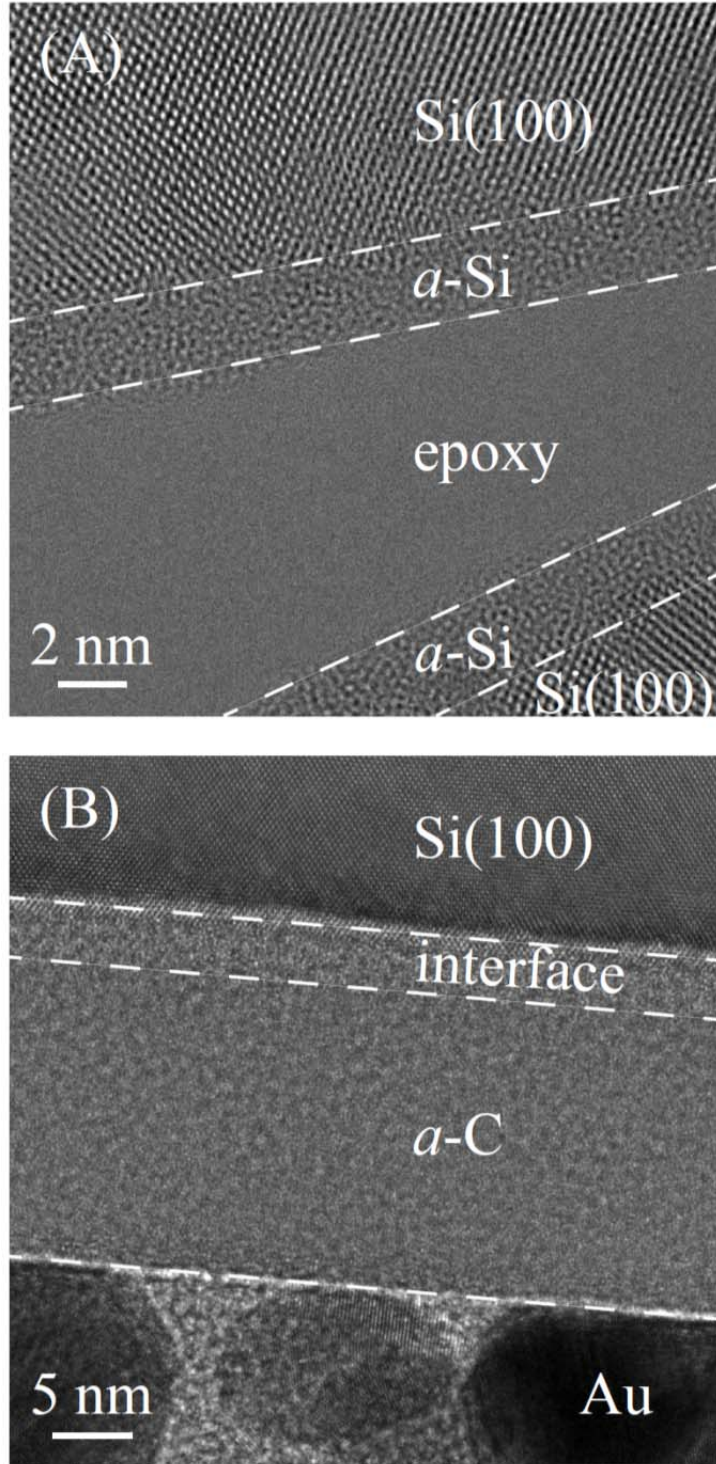


Figure 1

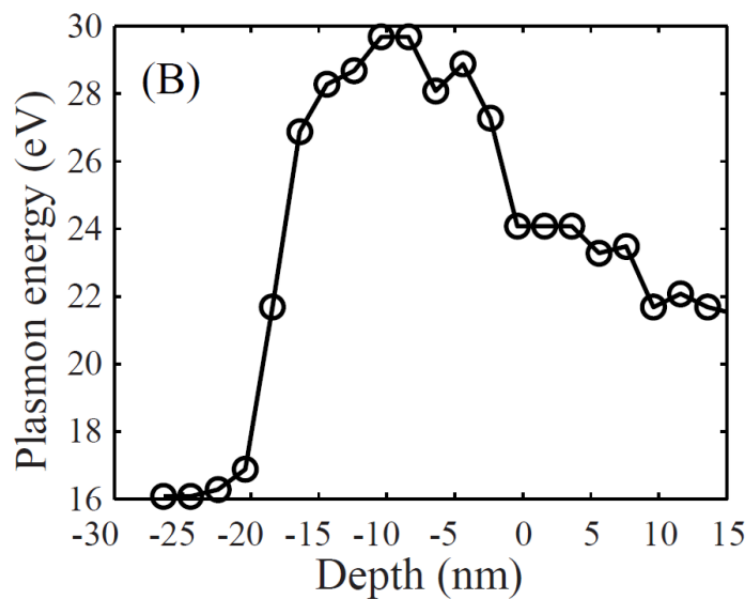
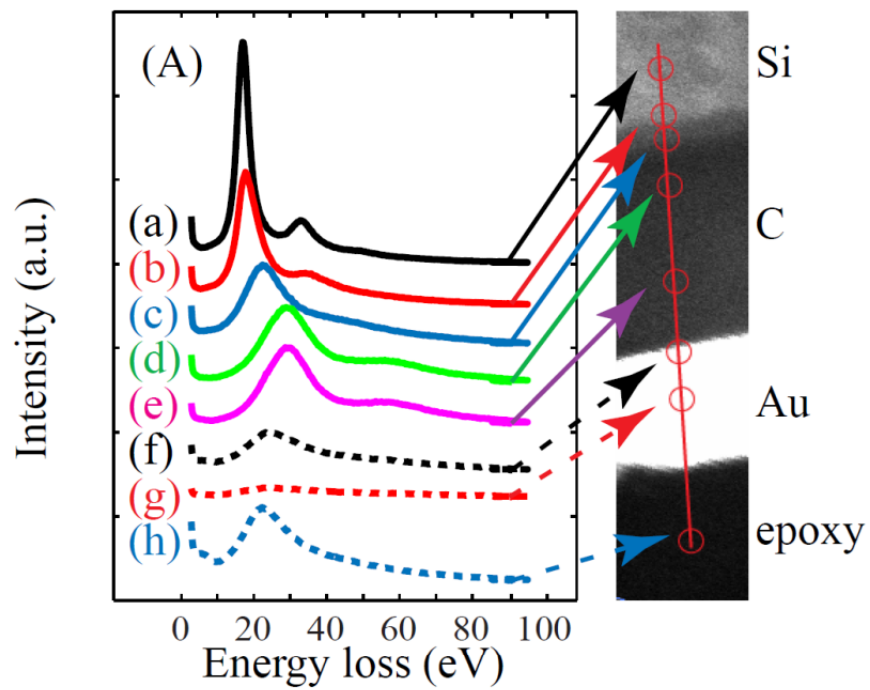


Figure 2

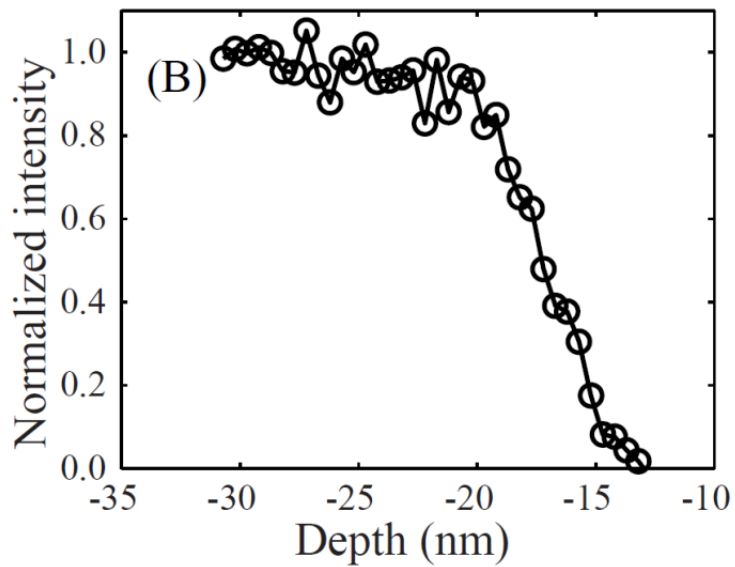
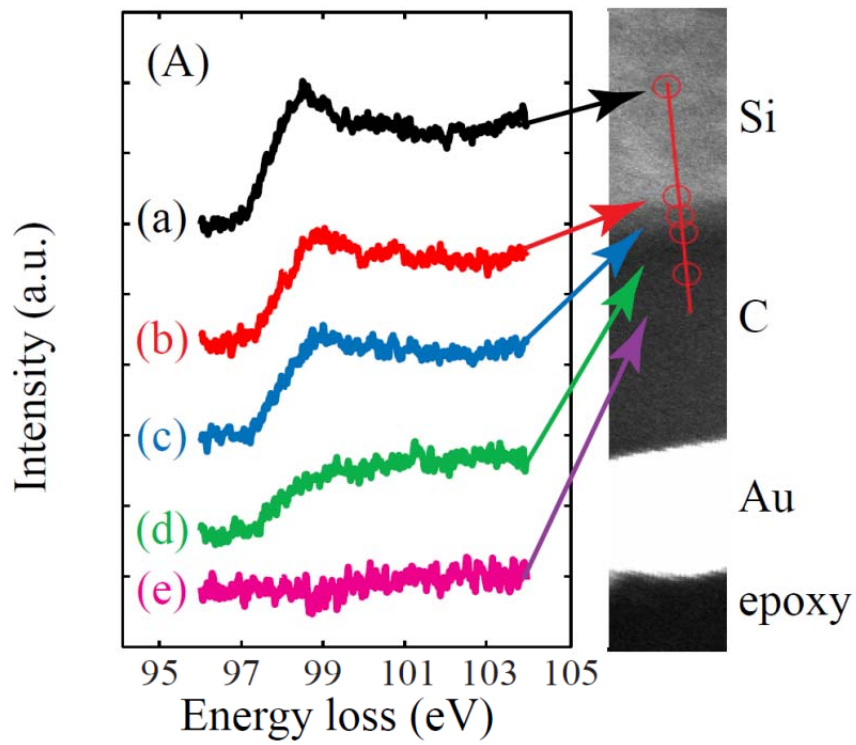


Figure 3

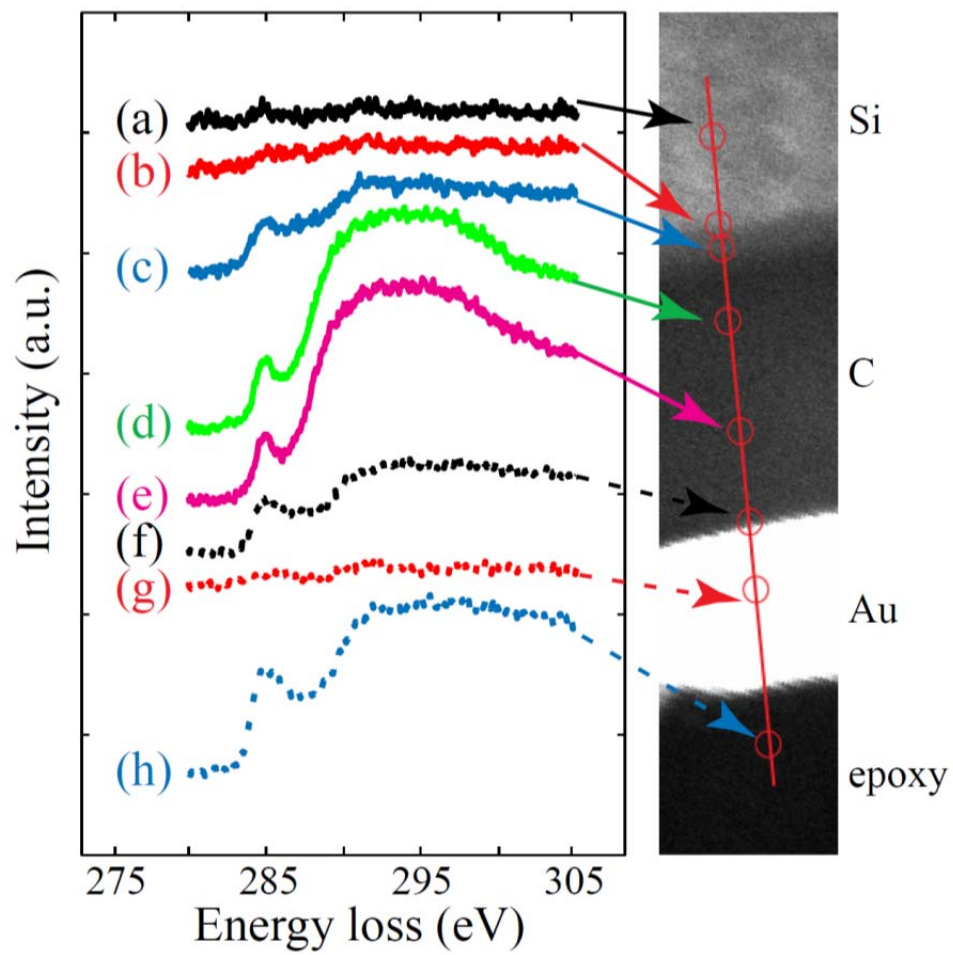


Figure 4

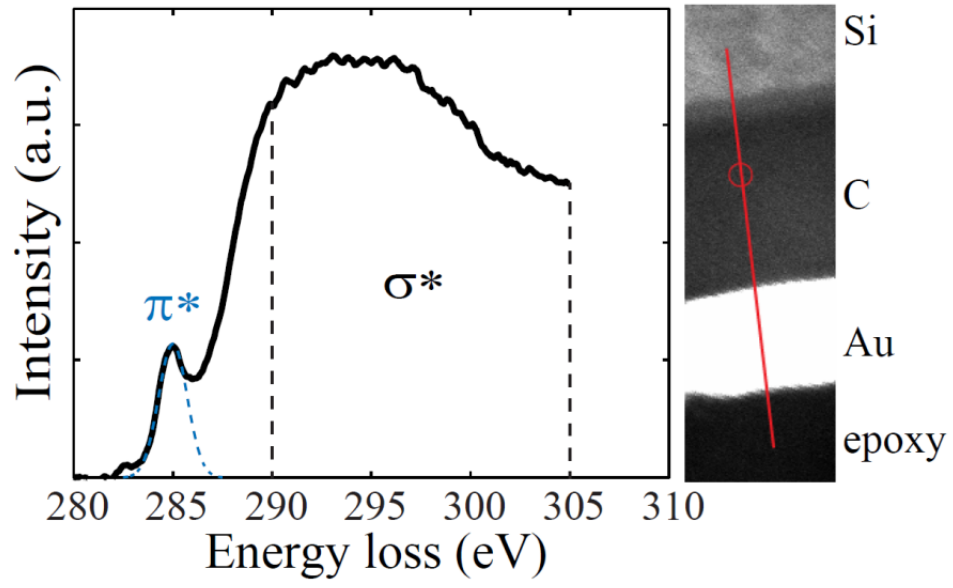


Figure 5

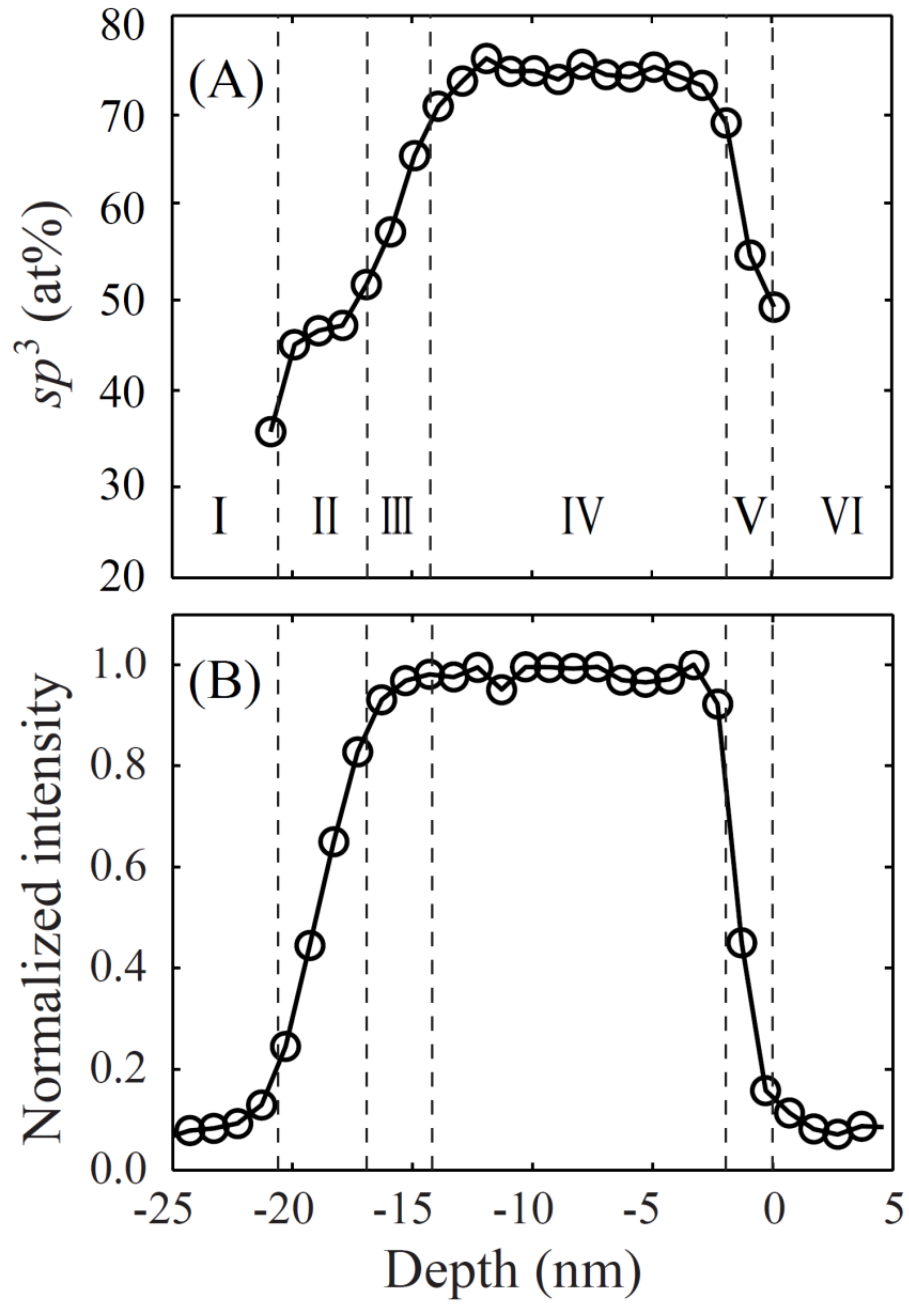


Figure 6

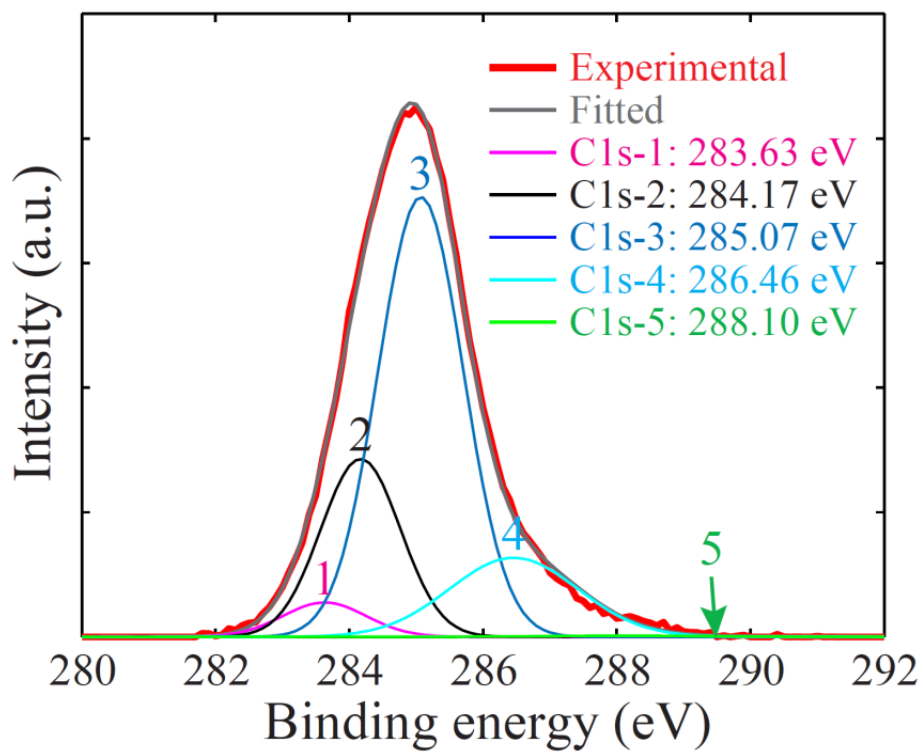


Figure 7